Volume Scanning Strategies for 3D Wind Retrieval from Dual-Doppler Lidar Measurements

Drechsel S., Mayr G.J., Chong M., Chow F.K.

Volume Scanning Strategies for 3D Wind Retrieval from Dual-Doppler Lidar Measurements

SUSANNE DRECHSEL AND GEORG J. MAYR

Institute of Meteorology and Geophysics, University of Innsbruck, Innsbruck, Austria

MICHEL CHONG

Laboratoire d'Aerologie, CNRS, Universite de Toulouse, Toulouse, France

FOTINI K. CHOW

Department of Civil and Environmental Engineering, University of California, Berkeley, Berkeley, California

(Manuscript received 14 May 2010, in final form 26 July 2010)

ABSTRACT

Dual-Doppler lidar volume scans for 3D wind retrieval must accommodate the conflicting goals of dense spatial coverage and short scan duration. In this work, various scanning strategies are evaluated with semi-synthetic wind fields from analytical solutions and numerical simulations over flat and complex terrain using the Multiple-Doppler Synthesis and Continuity Adjustment Technique (MUSCAT) retrieval algorithm. The focus of this study is to determine how volume scan strategies affect performance of the wind retrieval algorithm. Interlaced scanning methods that take into account actual maximum measurement ranges are found to be optimal because they provide the best trade-off between retrieval accuracy, volume coverage, and scan time. A recommendation for scanning strategies is given, depending on actual measurement ranges, the variability of the wind situation, and the trade-off between spatial coverage and temporal smoothing.

1. Introduction

Doppler lidars measure only the radial velocity component with typical along-beam resolution of 100 m. Very recently, simultaneous observations from two Doppler lidars have become available, which enables the measurement of two different radial wind components at the same time. By additionally using the continuity equation, the complete wind field can be retrieved. The quality of the retrieved wind field will, among other factors, depend on the scanning strategy used.

A variety of scanning and retrieval strategies exists for single-Doppler lidar measurements. At some airports, such as those in Hong Kong, Tokyo, and Paris, single-Doppler lidars are routinely applied for aircraft safety concerns. To detect hazardous wind situations caused, for example, by shear layers, special scanning strategies have been developed (e.g., Shun and Chan 2008). In research, single lidar measurements of radial wind (1D) fields are directly used, or 2D wind is estimated, for example, by the velocity–azimuth display (VAD) method (Browning and Wexler 1968) or in the case of channeled flow in valleys (e.g., Intrieri et al. 1990; Banta et al. 1992). Mostly, the lidars scan in limited azimuthal sectors or at relatively low elevations to retrieve, for example, boundary layer winds at horizontal planes (e.g., Chai et al. 2004).

For newly available dual-Doppler lidar observations, the limited spatial coverage or the long scan duration has mostly allowed *only* the determination of 2D wind vectors in vertical columns (e.g., Calhoun et al. 2006), or, based on retrieval methods, the 2D structures at horizontal and/or vertical planes (e.g., Newsom et al. 2008; Hill et al. 2010). Drechsel et al. (2009; hereafter D09) retrieved full 3D wind fields from dual-Doppler lidar measurements for quasi-stationary flow situations and scan patterns covering a large volume. The measurements were made during the field campaign of the Terrain-Induced Rotor Experiment (T-REX), which took place in the

Corresponding author address: Susanne Drechsel, Institute of Meteorology and Geophysics, University of Innsbruck, Innrain 52, A–6020 Innsbruck, Austria.
E-mail: susanne.drechsel@uibk.ac.at

DOI: 10.1175/2010JTECHA1495.1

Owens Valley, California, in March and April 2006 (Grubišić et al. 2008). Two Doppler lidars with baselines perpendicular to the valley axis were installed (Fig. 1) to observe the evolution of the 3D wind field of rotors, flow channeling, and valley wind systems, and other small-scale phenomena associated with mountain waves. D09 used a variational method for Cartesian 3D wind retrieval provided by Bousquet and Chong (1998) for radial wind observations from multiple-Doppler radars.

This Multiple-Doppler Synthesis and Continuity Adjustment Technique (MUSCAT) is suitable for application over both flat and complex terrain (Chong and Cosma 2000). D09 showed that the retrieval smoothed the 3D wind field both temporally and spatially. The scanning strategy, and especially the scan duration resulting from it, substantially influences the quality of the retrieved wind field.

In weather radar technology, the problem of fast but volume-covering scanning methods is well known. Different approaches have been developed to detect rapidly evolving systems or small-scale structures, which is particularly important for hazard warnings. One technically easy and effective realization is the interlaced scanning strategy, which is applied, for example, in the Swiss operational weather service. In a series of sectoral or full azimuthal scans at various elevation angles, the plan position indicators (PPIs) at every other elevation angle are skipped when elevation angles increase and scanned when elevation angles decrease. Vasiloff et al. (1987) investigated the interlaced scanning strategy for the Next Generation Weather Radar (NEXRAD). They showed that it allows the update frequency of wind shear warning time to double without compromising the evaluation of the storm attributes. Shapiro et al. (2003) could substantially improve retrieval error statistics by decreasing the volume scan intervals.

The lidar scanning strategy of T-REX mimicked the Swiss radar strategy, but consisted of only 10, instead of about 20, PPIs typical of radars. Despite fewer PPIs, each volume scan took about 16–20 min to complete because the signal processing is inherently different between Doppler lidar and Doppler radar (cf. Weitkamp 2005, 325–354; Meischner 2004, 1–51) and takes much longer for lidar. Thus, the relatively long scan duration hampered the investigation of rapidly evolving phenomena such as (sub)rotors, hydraulic jumps, etc. The resulting fields are affected by spatial smoothing caused by the lidar resolution with range gate lengths of about 100 m, the lidar scan strategy and, most of all, the data interpolation in the MUSCAT retrieval algorithm. It would be desirable to reduce both temporal and spatial smoothing by faster scans and improved spatial sampling coverage.

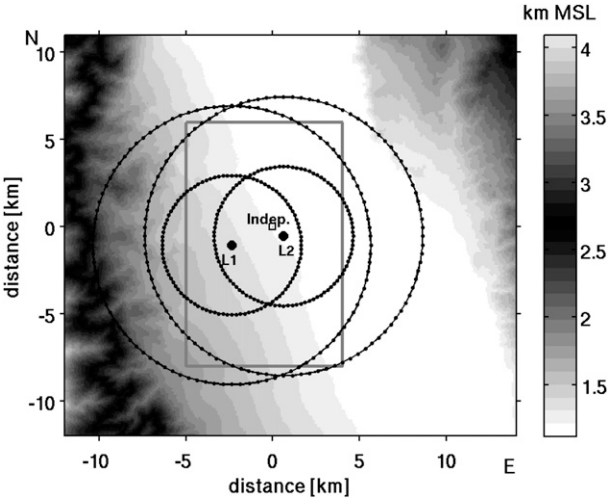

FIG. 1. Topography (shaded) of Owens Valley in the Sierra Nevada with coordinates centered at the town of Independence (Indep.). Additionally shown are the 4- and 8-km ranges of L1 and L2 lidars (circles), and the region of 3D wind retrieval shown in Fig. 4 (box).

A major goal of this investigation is to present dual-Doppler lidar volume scanning strategies that maximize spatial coverage and minimize scan duration in order to enable 3D wind retrieval of (quickly) changing wind situations. Because the true wind is not known from observations only, but also requires the performance of the strategies to be revealed, semisynthetic wind datasets are used for this study. They are described in the following section. The strategies and the data processing for the comparison are explained in section 3. Methods that require changes of the lidar system itself to shorten the scan duration, like beam multiplexing (e.g., Yu et al. 2007), are not considered in the present study. The results of the investigated strategies are presented in section 4 and discussed in section 5.

2. Wind data

Because no observations exist that describe the complete temporal evolution of the 3D wind field over a 3D region, we will use semisynthetic wind fields. The first dataset is from idealized, analytically determined wind fields. The second dataset consists of high-resolution (with a mesh width of 100 m) mesoscale model simulations over complex terrain for the T-REX campaign. The lidars are shifted roughly 2 km westward of their original position in the field for optimal exploitation of the model data. The first ''pseudo''-lidar L1 is situated about 2.4 km west and 1.1 km south of Independence, California (approximately at 1200 m MSL), at the foothills of the Sierra Nevada. The second pseudolidar L2 is

located approximately 0.6 km east and 0.5 km south of Independence, which results in a lidar baseline quasi-perpendicular to the valley axis (Fig. 1). To test the sensitivity of the retrieved winds to the alignment of the baseline, the lidars were also repositioned on a baseline parallel to the valley axis.

Both the analytical and the model wind datasets obey the continuity equation and represent the ''true atmosphere,'' which is scanned by two pseudo-Doppler lidars, L1 and L2. The scans follow all of the different proposed strategies. The ''observed'' radial wind fields are ingested into the variational algorithm MUSCAT (detailed in Bousquet and Chong 1998) to retrieve the Cartesian wind components u, v, and w of the 3D wind fields. MUSCAT interpolates the radial winds of both lidars onto a regular grid and then uses the continuity equation to retrieve 3D winds. The MUSCAT configuration with horizontal and vertical radii of influence of 1 and 0.5 km, respectively, for the interpolation onto a grid of 200-m mesh width in all directions, is the same as that described in D09. Centered at Independence, the retrieval domain extends 20 km × 20 km in the north–south and the west–east directions, and from 1 to 6 km MSL in the vertical direction.

The retrieved wind fields are compared to the original ''true atmosphere'' and thus reveal the performance of each scanning method. Because the strategies are finally checked against each other, an important, simplifying assumption is possible: the wind field is kept constant, that is, the flow is considered stationary during the time it takes to complete a volume scan. This assumption is necessary to compare scans with differing durations. Otherwise, even equal strategies of different durations would result in differing wind retrievals. In practice, this means that only the scanning strategy for which the scan duration is not longer than the time during which the phenomenon of interest is quasi stationary can be used. As another simplification, we do not simulate the effect of measurement errors.

a. Analytical wind fields

To focus on the scanning strategies instead of the performance of MUSCAT, two simple flow situations over flat terrain were chosen, which can be described analytically.

The first one (Chong and Testud 1996; Bousquet and Chong 1998) is a symmetrical cell case. A vertical west–east cross section at the location corresponding to Independence is shown (Fig. 2a). The wind field is characterized by relatively strong (horizontal) gradients in all wind components resulting from a divergence zone that is shifted with increasing height from northeast to southwest of the retrieval domain. The maximum

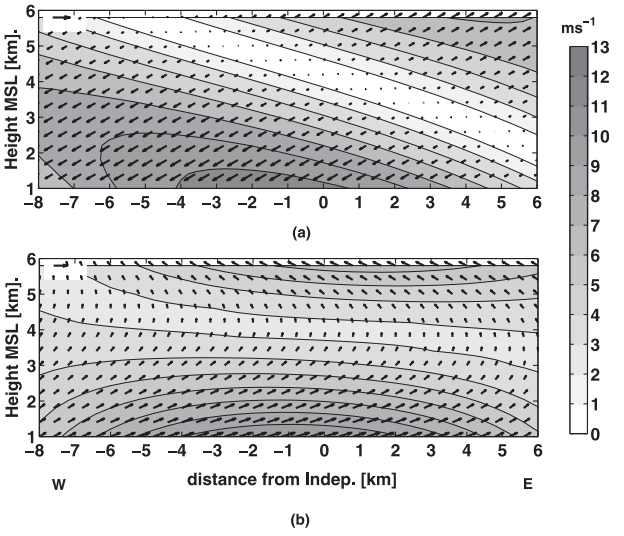

FIG. 2. Vertical west–east cross sections of analytical wind datasets. Horizontal wind (shaded with wind speed; m s^{-1}) of (a) a cell case at Independence and (b) a frontal case 1 km south of Independence. The reference wind vector at the top-left corner shows a 10 m s^{-1} westerly wind.

horizontal wind speed is approximately 8 m s^{-1}, with a median value of 4 m s^{-1}. Vertical wind velocities range from −6 to +7 m s^{-1}, with a downward motion of 1.1 m s^{-1} on average.

The second analytical wind field represents a frontal case as specified in Caillault and Lemaitre (1999). A vertical west–east cross section roughly at the location of lidar L1 is shown (Fig. 2b). Horizontal wind speeds are distributed between 1 and 13 m s^{-1}, with a median value of 5 m s^{-1}. Wind velocities are highest at 1 km AGL and at the top of the MUSCAT retrieval domain, which is at 6 km AGL. With increasing height, the wind direction turns from west to south to east. The vertical velocity ranges from −5 to +6 m s^{-1}, with a downward motion of 0.2 m s^{-1} on average. The horizontal gradients are weaker than that in the cell case.

b. Model wind fields

To also test the scanning strategies for more realistic wind situations and over complex terrain, three other wind fields (1800, 1855, and 1950 UTC) were extracted from an Advanced Research Prediction System (ARPS) model simulation of the 30 March 2006 T-REX case. The grid in the smallest nested domain has a horizontal mesh width of 100 m and 100 sigma levels in the vertical, and is centered at Independence. With 192 grid points in both north–south and west–east directions, the nested grid covers 19.2 km × 19.2 km. The vertical spacing between the levels is about 14 m at the bottom and 180 m at 6 km MSL. Although they are real model data, the wind

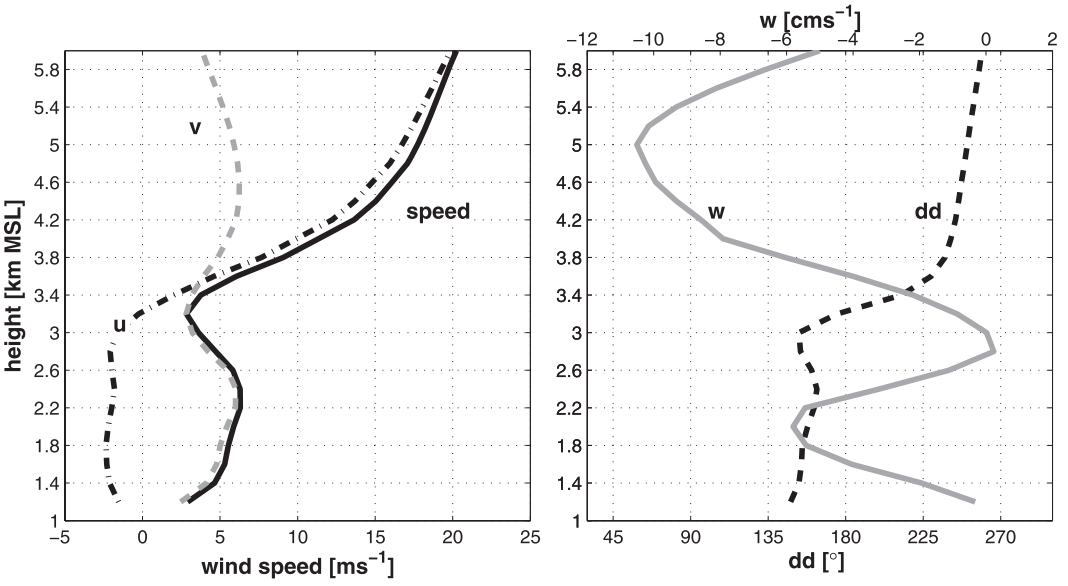

FIG. 3. Profiles of (left) horizontal wind speed (solid), wind components u (dashed–dotted) and v (dashed), and (right) w (solid) and wind direction dd (dashed) of the ARPS wind field at 1950 UTC 30 Mar 2006, horizontally averaged over the ARPS domain.

fields are called semisynthetic, because verification against true conditions is not the focus of this study.

The ARPS wind field is characterized by a moderate (mostly 3–6 m s^{-1} in the horizontal average) southeasterly flow in the valley below 3 km MSL (Fig. 3). Above crest level, wind speed increases to 20 m s^{-1} and shifts direction to a westerly flow at 6 km MSL, which is the top of the MUSCAT retrieval domain. Vertical wind speed at grid points ranges mainly between -1 and $+1$ m s^{-1}, but also reaches absolute values of 5 m s^{-1}. The horizontal cross sections of horizontal and vertical wind speeds at 4.6 km MSL (Fig. 4) indicate weak undulations.

3. Scanning strategies

Various volume scan strategies are applied to sample the semisynthetic wind fields. Because the maximum lidar range strongly depends on aerosol content, three typical lidar ranges are used. The strategies mainly differ in the number and elevation angles of the PPIs, but also in the azimuthal increment of the PPIs. For each strategy, radial velocities V_r are computed from the Cartesian wind components of the mesoscale model and the analytical solutions. These "pseudo-measurements" of V_r are ingested into MUSCAT to retrieve Cartesian wind components again. The retrieved fields based on the different strategies are compared to the original semisynthetic wind fields.

The focus of this study is on the performance of the volume scans. Four different scan types with respect to the choice of elevation angles are investigated: a high-resolution (HR) reference scan; the volume scan strategy applied during the T-REX campaign (TX); a strategy that ensures volume coverage based on parameter settings of the retrieval algorithm (VC); and a strategy where the volume is scanned in a sinusoidal pattern (SW). The HR scan with 1° steps in both azimuth and

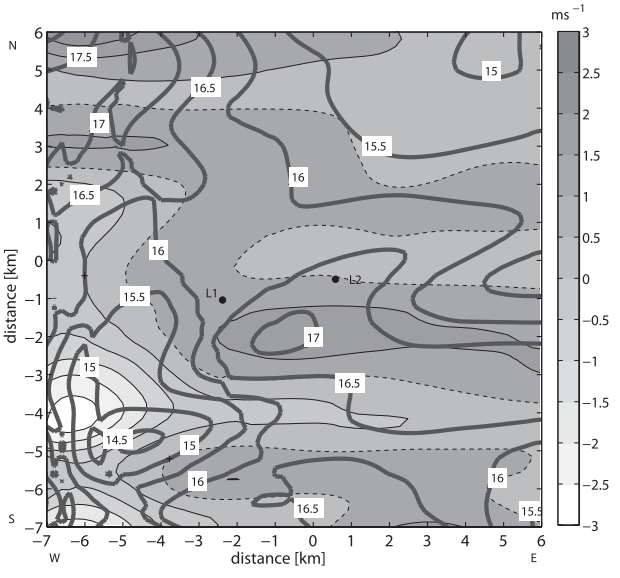

FIG. 4. Horizontal cross sections of the vertical wind component w (shaded; m s^{-1}; zero line is dashed) and horizontal wind speed (black contours, m s^{-1}) of ARPS wind field at 4.6 km MSL (i.e., above crest level) at 1950 UTC 30 Mar 2006. L1 and L2 mark the positions of the two lidars.

TABLE 1. Name, elevation angles of the PPIs, scan duration T, and substrategies of the scan strategies for the three different lidar ranges. HR is the high-resolution reference scan. TX-m is the strategy applied during the T-REX field campaign with 3° azimuthal increments for the PPIs at elevation angles written in bold letters and 5° azimuthal increments for the other PPIs. TX-h is the T-REX half-scan, consisting only of those PPIs written in bold letters. TX-m6 and TX-h6 are the same but with 6° azimuthal increments instead of 3° and 5°, respectively. Half-scans VC-h1 (bold) interlaced with VC-h2 (italic) build a complete VC-c scan. SW-4 and SW-8 are sinusoidal wave scans, with 6° of azimuthal increment.

Name	PPI elevation angles (°)	T (min)	Substrategies
HR	1–89	538.4	
TX-m	**3** **6** **10** 14 **18** 22 **27** 32 **45** 60	17.3	**TX-h**, TX-m6, **TX-h6**
	Range: 4 km horizontally and vertically (h4v4)		
VC-c-0	**7** *21* **36** *54*	4.2	**VC-h1–0**, *VC-h2–0*
VC-c-10	**6** *19* **33** *48* **68**	5.2	**VC-h1–10**, *VC-h2–10*
VC-c-20	**6** *17* **29** *42* **57**	5.2	**VC-h1–20**, *VC-h2–20*
VC-c-30	**5** *15* **25** *36* **48** *64*	6.3	**VC-h1–30**, *VC-h2–30*
VC-c-40	**4** *12* **21** *30* **40** *51* **66**	7.3	**VC-h1–40**, *VC-h2–40*
VC-c-50	**4** *11* **18** *25* **33** *41* **50** *62*	8.4	**VC-h1–50**, *VC-h2–50*
	Range: 8 km horizontally and 4 km vertically (h8v4)		
VC-c-0	**3** *10* **17** *24* **33** *46* **67**	7.3	**VC-h1–0**, *VC-h2–0*
VC-c-10	**3** *9* **15** *21* **28** *37* **51**	7.3	**VC-h1–10**, *VC-h2–10*
VC-c-20	**3** *8* **13** *18* **24** *31* **41** *55*	8.4	**VC-h1–20**, *VC-h2–20*
VC-c-30	**3** *8* **10** *18* **23** *29* **37** *47* **62**	9.4	**VC-h1–30**, *VC-h2–30*
VC-c-40	**2** *6* **8** *14* **18** *22* **26** *32* **39** *49* **63**	11.5	**VC-h1–40**, *VC-h2–40*
VC-c-50	**2** *5* **8** *11* **14** *17* **20** *23* **27** *32* **38** *46* **56**	13.6	**VC-h1–50**, *VC-h2–50*
	Range: 8 km horizontally and 6 km vertically (h8v6)		
VC-c-0	**3** *10* **17** *24* **31** *39* **48** *60*	8.4	**VC-h1–0**, *VC-h2–0*
VC-c-10	**3** *9* **15** *21* **27** *34* **41** *50* **61**	9.4	**VC-h1–10**, *VC-h2–10*
VC-c-20	**3** *8* **13** *18* **24** *30* **36** *42* **50** *60*	10.5	**VC-h1–20**, *VC-h2–20*
VC-c-30	**3** *8* **13** *18* **23** *28* **33** *38* **44** *51* **60**	11.5	**VC-h1–30**, *VC-h2–30*
VC-c-40	**2** *6* **10** *14* **18** *22* **26** *30* **34** *39* **44** 50 **57** *66*	14.7	**VC-h1–40**, *VC-h2–40*
VC-c-50	**2** *5* **8** *11* **14** *17* **20** *23* **26** *30* **34** 38 **42** *47* **53** *60* **68**	17.8	**VC-h1–50**, *VC-h2–50*
SW-4	Four full rotations, with three sinus waves in total, between 1 and 54/67/60 for h4v4/h8v4/h8v6	10.8–10.9	
SW-8	Eight full rotations, with seven sinus waves in total, between 1 and 54/67/60 for h4v4/h8v4/h8v6	21.3–22.1	

elevation takes more than 500 min, which is impractical for real application, but is used as a benchmark against which the other scan strategies are compared. Except for the HR scan, there are substrategies, which are described and summarized in Table 1.

a. T-REX scan pattern

In the T-REX field campaign, the main volume scan pattern (TX-m) consisted of a first set of PPIs at elevation angles of 3°, 6°, 10°, 18°, 27°, and 45°, with an azimuthal increment of 3°, followed by a second set of PPIs at 14°, 22°, 32°, and 60°, with an azimuthal increment of 5°. The TX half-scan (TX-h) consisted only of the PPIs at 3°, 6°, 10°, 18°, 27°, and 45°, with an azimuthal increment of 3°. For an easier comparison with VC and SW scans, TX-m and TX-h scan strategies are also tested with 6° azimuthal increment, labeled TX-m6, and TX-h6, respectively.

b. Volume coverage scan pattern

In D09, a method was proposed to obtain a range-dependent scan strategy that ensures volume coverage when combined with MUSCAT. The elevation angles of the scans are spaced such that the ellipsoids with half-axes given by the radii of influence r_v (vertical) and r_h (horizontal) exactly touch each other at the actual (previously determined) maximum range $r_{\max}$ of two vertically successive beams (see Fig. 5). The angle increment $\Delta\theta_i$ between two successive beams can be estimated from the implicit equation

$$r_v^2\left[\sin\left(\frac{\Delta\theta_i}{2}\right)\sin\left(\frac{\Delta\theta_i}{2}+\varepsilon_i\right)\right]^2 + r_h^2\left[\sin\left(\frac{\Delta\theta_i}{2}\right)\cos\left(\frac{\Delta\theta_i}{2}+\varepsilon_i\right)\right]^2 - \left(\frac{r_v r_h}{r_{\max}}\right)^2 = 0, \quad (1)$$

where ε_i is the elevation angle of PPI_i. For the lowest PPI above ground ($i = 1$), it is determined by $\sin(\varepsilon_1) = r_v/r_{max}$ The implicit equation can be solved numerically or graphically. To investigate whether 3D wind retrieval can also profit from interlaced scanning strategies, the VC scans are divided into two parts with alternating PPI elevations: VC-h1 and VC-h2, which can be interlaced to build the composite scan VC-c described above. When only the half-scans are used the ellipsoids no longer touch at r_{max}, and spatial coverage of these VC-h scans becomes incomplete. Therefore, additional strategies are designed with smaller steps between the elevation angles. The $\Delta\theta_1$ computed according to Eq. (1) is reduced by 10%, 20%, 30%, 40%, or 50%, respectively, before calculating the $\Delta\ \theta_i$. Consequently, the ellipsoids of the VC-c composite scans *overlap* at r_{max}. When $\Delta\theta_i$ is reduced by 50%, the ellipsoids of the half-scans again touch each other at r_{max}. The half-scans are labeled VC-h1–10 and VC-h2–10, the corresponding interlaced scan is VC-c-10, etc., where the last number is the percentage reduction of $\Delta\theta_i$ (i.e., the overlap).

c. Sinusoidal scan pattern

The SW scans consist of 4 (SW-4) or 8 (SW-8) full azimuthal rotations with continuously upward- and downward-changing elevation angles, so that the beam follows three and seven sine waves, respectively. The maximum elevation angle, which corresponds to the double amplitude of the sine wave, is equal to that calculated for the VC scans for the different ranges. The sinusoidal scan pattern should enable faster horizontal *and* vertical coverage of the volume than PPI-based scans.

d. Azimuthal increments

Including the HR scan, there are 25 scan strategies in total, as summarized in Table 1. For all of them, ''step and stare'' scanning instead of continuous rotation is assumed. This means that the lidar beam temporarily stops at a given position defined by its azimuth and elevation angles and samples for a certain period (called beam-averaging time, which is on the order of 1 s) at this fixed direction. The step-and-stare mode allows for increasing azimuthal angle increments, that is, faster PPI scans, without increasing statistical error (O. Reitebuch, DLR, 2009, personal communication). However, it should be mentioned that most systems in use today do not yet employ step and stare [an exception is the Doppler lidar of the Deutsches Zentrum für Luft- und Raumfahrt (DLR)].

For the TX-m scan pattern, the azimuthal increments are set similarly as those during the T-REX field campaign (cf. section 3a); TX-h consists only of those six PPIs with 3° increments. For the other scan patterns, the azimuthal increment is 6°. This ensures that at the applied maximum lidar ranges in this study, the (interpolation) ellipsoids overlap about 50% in the horizontal, which is the same as for the VC-c-50 scans in the vertical.

e. Scan duration

The total volume scan duration T results from the number of different azimuth and elevation angles and the beam-averaging time, plus time for changing the elevation angle. For this study the beam-averaging time was set to 1 s, similar to the T-REX lidar dataset used in D09. For elevation changes a 3-s duration is assumed. While the scan duration is constant for strategies with constant structures (HR and TX scans), it changes for strategies that depend on maximum range (VC and SW scans).

f. Measurement range

Because of weak backscatter signals in the case of a low aerosol load in the atmosphere, the *actual* maximum range of the lidar is often much smaller than the maximum range given by its technical settings. During the T-REX campaign, the technical maximum ranges were 8 [Arizona State University (ASU) lidar] and 11 km (DLR lidar), respectively, with the actual maximum ranges falling between 3 and 11 km. Therefore, three different cases of lidar maximum ranges are assumed in this study: 4 km in both horizontal and vertical directions (h4v4), and the combinations of 8 km × 4 km (h8v4) and 8 km × 6 km (h8v6), respectively, in the horizontal–vertical directions. The vertical measurement height of 4 km is the upper limit of the depths of boundary layers with sufficient aerosol backscatters. At even higher altitudes, thin clouds might provide a sufficiently strong backscattering signal.

g. Processing of the wind data

The stepwise processing of the wind data is depicted schematically in Fig. 6. For all scan strategies, radial velocities V_r are computed from the Cartesian wind components of the semisynthetic fields from the model and the analytical solutions for the scan coordinates within the assumed maximum ranges. Here, V_r is calculated for the center of each lidar range gate, which has a length of 100 m. While V_r can be determined exactly at any location from the analytical fields, the wind components of the ARPS data have to be interpolated

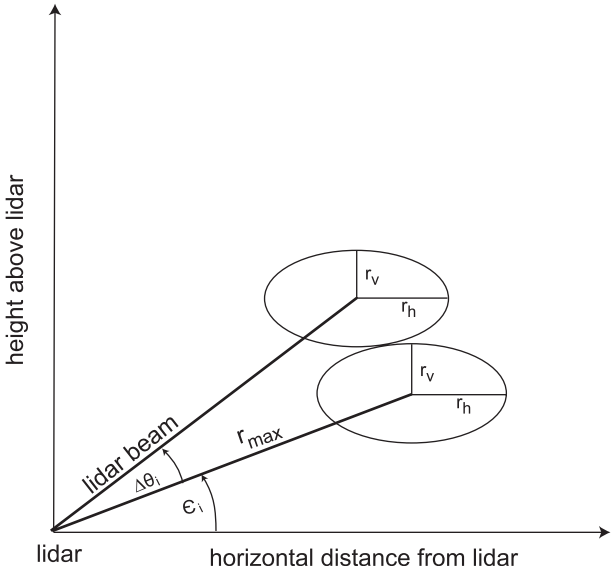

FIG. 5. Schematic depiction of the volume coverage scan pattern. Ellipsoids with half-axes determined by the radii of influence r_v and r_h of the 3D wind retrieval algorithm at two (vertically) successive beams touch each other at the distance r_{max}. The lower beam is at elevation angle ε_i, with an elevation step $\Delta\theta_i$ to the upper beam.

onto the scan coordinates from the surrounding eight model grid points before V_r is determined. MUSCAT retrieves the Cartesian wind components from these pseudo-measurements on a regularly spaced grid, which is different from the original ARPS grid. Thus, for comparison of the original ARPS data to the MUSCAT-retrieved data, the ARPS wind components are interpolated to the MUSCAT grid. These interpolations lead to unavoidable inaccuracies. Though the analytical wind components can be calculated exactly for the MUSCAT grid coordinates, the internal MUSCAT interpolation also creates differences for the analytical fields. The HR scans described in section 3 provide a reference point.

4. Results

There are three requirements for a ''good'' scanning strategy: small differences D between the original fields and the retrieved fields, a large size of the retrieved field represented by the number of grid points N for which wind could be retrieved, and short scan duration T. To reveal the performance independent of the modifications of the wind fields introduced by interpolation used in the MUSCAT retrieval algorithm, the results of the high-resolution HR scans are scrutinized first and used as reference for the other strategies.

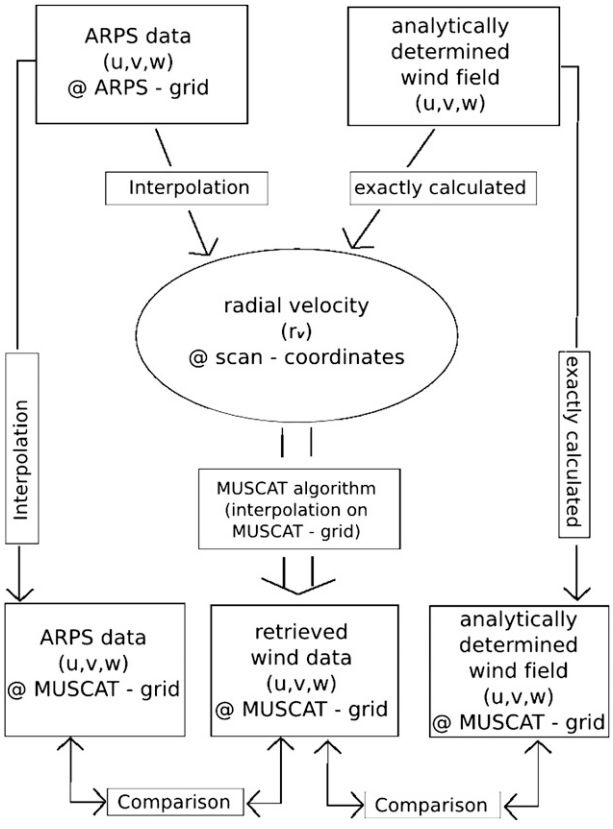

FIG. 6. Schematic depiction of the stepwise data processing.

a. Performance of HR reference scans

Though the HR scan pattern with azimuth and elevation steps of 1° perfectly covers the half space within the given maximum range, it is inapplicable in practice because of its scan duration of several hours. The results are only used to highlight the modifications caused by the retrieval algorithm and to serve as baseline for the wind fields retrieved from the other scanning strategies.

For the low assumed lidar range of 4 km in both the horizontal and vertical directions (h4v4), the corresponding volume approximately extends 6 km × 8.5 km × 4 km in the west–east, north–south, and vertical direction. For the middle (large) lidar range h8v4 (h8v6), wind is retrieved in a box of roughly 8 km × 13 km × 4 km (8 km × 13 km × 6 km). With the 200-m MUSCAT mesh used, the number N of retrieved values increases to 58 000 when using the analytical wind fields over flat terrain. Using the ARPS dataset, N is about the same over flat terrain for the low and medium ranges, but only 47 000 for the large lidar range resulting from the complex terrain.

The differences D between the original and the retrieved wind fields at the MUSCAT grid points are caused by smoothing within the retrieval algorithm. The stronger the gradients within the initial wind field, the

stronger the smoothing and the larger the differences. Furthermore, the median value of the differences $\overline{D}$ and the standard deviation σ (D) also depend on the magnitude of the velocity of the initial field.

For all wind components of the analytical wind datasets at all lidar ranges, $\overline{D}$ is between -0.1 and $+0.1$ m s^{-1}, revealing that the retrieved data are unbiased. The standard deviation $\sigma(D)$ of horizontal wind components u and v is less than or equal to 0.7 m s^{-1}, independent of the lidar range. For the vertical component w, $\sigma(D)$ slightly increases with an increasing horizontal and vertical range, from approximately 1.0 (0.7) to 1.7 (1.3) m s^{-1} for the cell (frontal) case.

Similar results are obtained for $\overline{D}$ when the ARPS model data are used. Ranging from -0.1 to $+0.2$ m s^{-1}, the retrieved wind components from the ARPS datasets are also virtually unbiased. At all assumed ranges, $\sigma(D)$ is less than 1 m s^{-1} for u, v, and w. While the deviations of the horizontal wind are slightly higher for ARPS data than for analytical data, they are lower for the vertical wind, with $\sigma(D)$ ranging from 0.3 to 0.6 m s^{-1}. The reasons are the different distributions of the horizontal and vertical wind velocities and the weaker gradients in the ARPS dataset.

When the lidar baseline is rotated from perpendicular to parallel to the valley axis, $\sigma(D)$ is slightly higher for the u component and slightly lower for the v component for the *low vertical* lidar ranges (h4v4 and h8v4) where the v component dominates. It is exactly the opposite for the larger vertical range (h8v6), when the lidars also measure at elevations where the u component dominates.

b. Performance of TX, VC, and SW scan patterns

The performance of the T-REX-like scanning strategies TX, the volume coverage scan pattern VC, and the sinusoidal scan pattern SW, is analyzed by the three criteria: (i) relative standard deviation $\sigma_{\text{rel}}(D) = \sigma(D)/\sigma_{HR}(D)$ of the wind components, (ii) the relative size $N_{\text{rel}} = N/N_{\text{HR}}$ of the retrieved fields, once both are normalized with the reference scan HR, and (iii) the relative scan duration $T_{\text{rel}} = T/T_{\text{TX–m}}$, normalized with the TX-m scan.

In general, good performance is obtained by using the volume coverage composite (VC-c) scans with overlap angles of 20%–40%, the halves of the VC-c scans with overlap angles of 40% and 50%, and the T-REX scan pattern with an azimuthal increment of 6° (TX-m6). The SW-4 scans and the two halves of the interlaced scans VC-h1 and VC-h2 ≤ 20 (i.e., with overlap angles of no more than 20%) perform poorly, with up to 30 times the standard deviations of the HR scan. The overall assessment regarding the difference between the original and the retrieved wind, the scan duration, and the size of the retrieved fields are summarized in Figs. 7a–c and 8a–c. For each of the three measurement ranges, the figures show the overall ranking position of each strategy, using the analytical and model datasets, respectively. The ranking position is calculated from total "penalty" points averaged over the five parameters $\sigma_{\text{rel}}(D)$ of the three wind components T_{rel} and the reversed field size $1/N_{\text{rel}}$. For a given parameter (and a given dataset at a given lidar range), the range of the relative results of all scans is divided into 24 equally spaced bins. The penalty points for a given scan then correspond to bins (number) 1–24, according to the result of the respective scan.

In that overall ranking, the volume-covering composite scan VC-c with an overlap angle of at least 30% compromises best between the three design criteria at the short measurement range h4v4 (cf. Figs. 7a and 8a). The SW-4 scan, as well as the halves of the volume-covering scans with overlap angles of less than 40%, performs poorly. Though the scan is fast, the retrieved fields are small and of an inadequate quality. When the horizontal measurement range increases to h8v4, the SW scans, and especially the SW-4 scan, as well as the TX-h scan, also emerge to be inappropriate for a 3D wind retrieval. This is due to either a large $\sigma_{\text{rel}}(D)$ (VC-h $\leq$ 20), a long scan duration (SW-8), or a small retrieved fields (VC-h ≤ 10), or combinations thereof (SW-4, TX-h). Again all of the VC-c scans, VC-h ≥ 40, and TX-m6 provide the best results (cf. Figs. 7b and 8b). Finally, at the large horizontal and vertical range h8v6, the assessment of most strategies does not change much compared to that of h8v4 (cf. Figs. 7c and 8c). However, the VC-c-50 is ranked lower because of its long scan duration, whereas the VC-h-30 does better.

Scrutinizing the design criteria for a satisfactory scan pattern in more detail unveils that the ranking of the strategies depends on both the actual measurement range and the spatial variability of the wind field.

1) SHORT RANGE

Using the analytical wind fields at the h4v4 measurement range, most of the strategies perform rather similarly, with the retrieved fields barely different from those using the HR scan. Thus, $\sigma_{\text{rel}}(D)$ varies around 100% for most of the scans. The unusual exception, with up to tenfold greater values for $\sigma_{\text{rel}}(D)$, is the VC-h ≤ 20 scans. With the relatively smooth ARPS wind fields, the performance of the strategies regarding $\sigma_{\text{rel}}(D)$ is more distinct. The largest values, that is, the worst results, are found for the half-scans VC-h ≤ 30 (either VC-h1 or VC-h2, or both). The lowest $\sigma_{\text{rel}}(D)$ (generally less than 200% of the HR scan for all wind components) is obtained by the composite scans VC-c ≥ 30, all of the TX scans, and the SW-8 scan. With respect to the field size

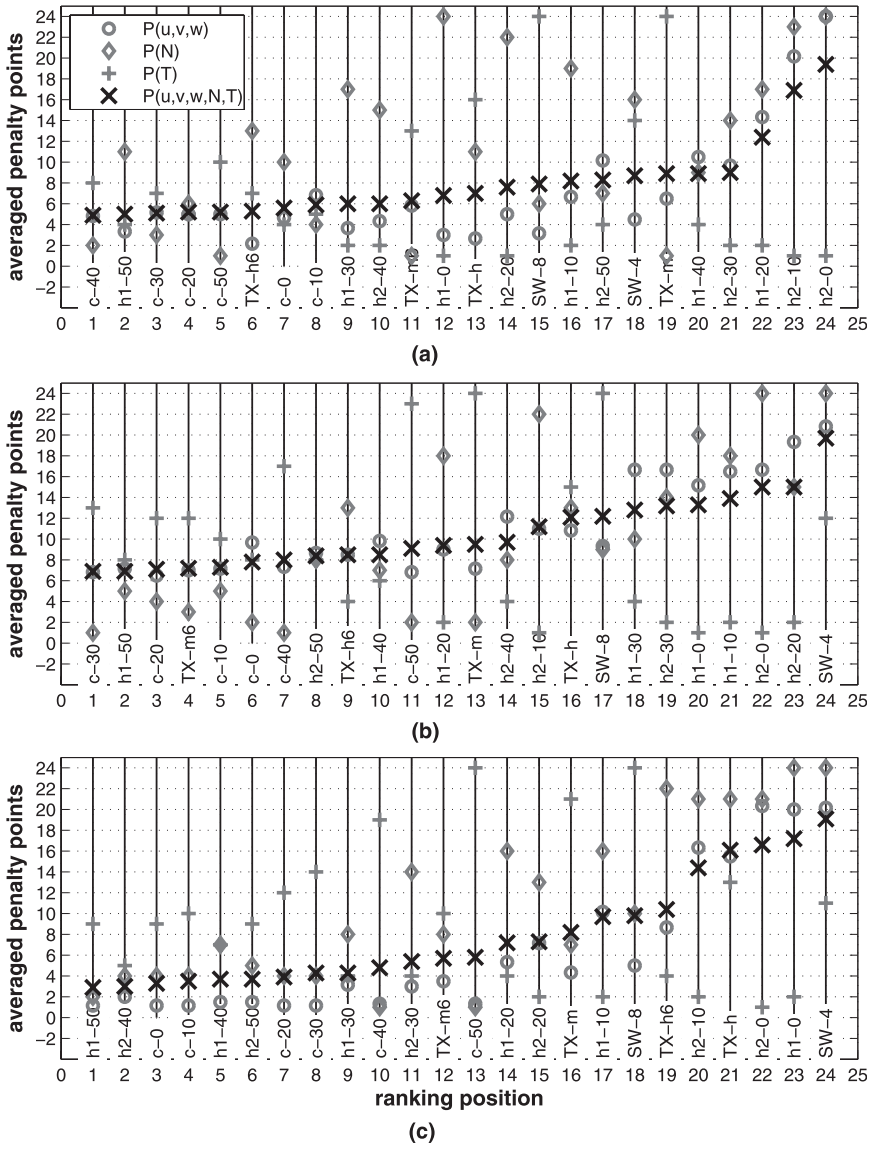

FIG. 7. Ranking positions of the different scanning strategies (cf. Table 1) using both analytical datasets for the (a) h4v4, (b) h8v4, and (c) h8v6 measurement ranges. The *x*'s indicate the mean penalty points P for the performance regarding the five parameters $\sigma_{\text{rel}}(D)$ of u, v, and w; the relative scan duration T_{rel}; and the relative field size N_{rel}. Penalty points for $\sigma_{\text{rel}}(D)$ of u, v, and w only (open circles); T_{rel} only (diamonds); and T_{rel} only (plus signs). See text for more details. The names of the volume-covering scans are shortened by omitting "VC-".

N_{rel}, the SW-4 scan and VC-h ≤ 20 are the worst, not even reaching 50% of the HR scan. The best results, with approximately 80%, are achieved by the VC-c ≥ 30 strategies and the TX-m scan. However, they have a long scan duration T_{rel}. Depending on the overlap angles, the fastest scans are the VC-h scans, with T_{rel} ranging from 12% to 24%, followed by the VC-c scans with 24%–48%, the TX-h6 scan with 36%, and the SW-4 scan with 46%. The slowest scans are the SW-8 (124%) and the TX-m scan itself.

2) INTERMEDIATE RANGE

With the h8v4 measurement range, the SW-4 scan and VC-h ≤ 30 result in the largest $\sigma_{\text{rel}}(D)$ with both the analytical and the model dataset. While the SW-8 scan is average using the analytical wind fields, it is almost the worst with the ARPS data. For both datasets, the lowest $\sigma_{\text{rel}}(D)$ are found for VC-c ≥ 20, TX-m, and the TX-m6 scans. Again, the ranking of the good scans is less distinct using the analytical dataset. Regarding N_{rel}, all

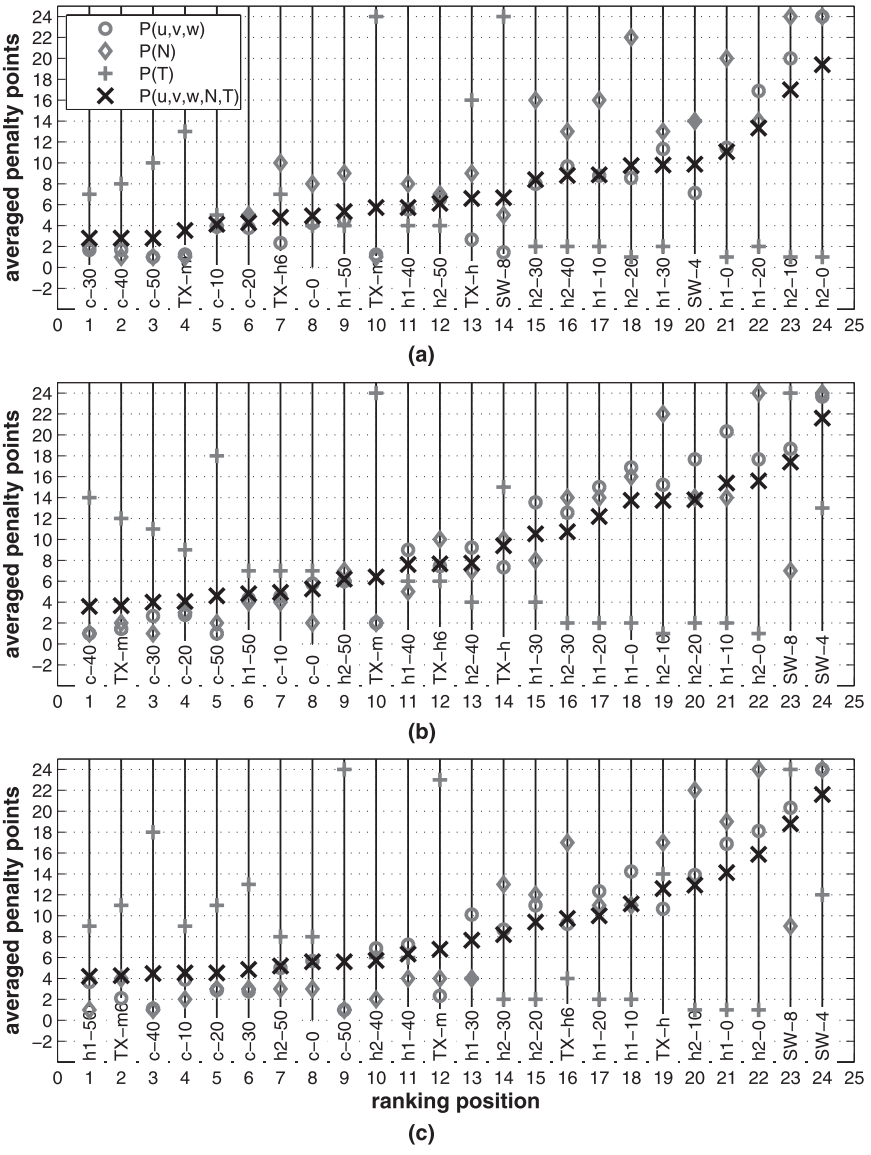

FIG. 8. As in Fig. 7, but for the three ARPS wind fields.

strategies reach more than 50% of the HR scan field size, except for the SW-4 scan (approximately 40%). VC-c $\geq$ 20, TX-m, and the TX-m6 scan are best, with about 90%. Because the scan patterns of the VC and the SW scans depend on the measurement range, their scan duration increases, while it is constant for the TX scan pattern. Thus, the slowest scans are the VC-c-50 scan and, again, the TX-m and the SW-8 scans, with T_{rel} ranging from 79% to 128%, while for VC-h $T_{\text{rel}} \leq 50\%$.

3) LARGE RANGE

Using the model datasets at the largest measurement range h8v6 results in a similar ranking for $\sigma_{\text{rel}}(D)$ as with the h8v4 measurement range. For the analytical datasets, again the SW-4 and the VC-h $\leq$ 20 are the worst, but now the SW-8, TX-h, and TX-h6 scans perform poorly also. All of the composite VC-c scans and the half-scans VC-h $\geq$ 40 perform best. With the SW-4, VC-h $\leq$ 10, TX-h, and TX-h6 scans, N_{rel} is smallest, ranging from 42% to 58% over flat terrain for the analytical dataset, and from 42% to 67% over complex terrain (model dataset). The largest retrieved wind fields are provided by the VC-c scans, followed by VC-h $\geq$ 40, with 84%–99% of that of the HR scan. However, the scan duration of the VC-c-50 scan now slightly exceeds that of the TX-m scan. The VC-h $\leq$ 30 and the TX-h6 scans are the fastest, with $T_{\text{rel}} \leq 36\%$.

5. Summary and discussion

In this study, the performance of various scanning strategies for 3D wind retrieval from dual-Doppler lidars is investigated. Radial velocities from pseudoscans in both the model (ARPS) and analytical wind fields are ingested into the MUSCAT retrieval algorithm.

There are two possible reasons for deviations of retrieved fields from the original (stationary) wind fields: insufficient spatial coverage of the scan strategy and spatial smoothing by the algorithm. The latter is caused by interpolation of all data inside a horizontal and vertical radius of influence onto the retrieval grid, and by the low-pass filter applied in the algorithm. Furthermore, the accuracy of the retrieved wind components depends on the angles of incidence of the lidars. Ideally, the angles would be perpendicular to each other. Thus, errors increase with decreasing distance to the baseline between the lidars, where both lidars are scanning with almost the same angle (cf. Fig. 2 in Chong and Bousquet 2001). In this study, we focus on the errors that depend on the scan strategy only.

A high-resolution (HR) scan is used to assess the differences D of the reproduced wind components u, v, and w to the original wind fields. For the three different assumed lidar ranges, the standard deviations of the differences $\sigma(D)$ are less than 1 m s^{-1} for the quasi–real case flow situation of the ARPS model. Turning the lidar baseline by 90° reveals that the differences slightly decrease for the component parallel to the baseline. The analytical wind fields represent a cell case and a frontal case, respectively. Compared to the model dataset, the horizontal wind speed is slightly lower, but the spatial gradients are stronger, and the vertical velocity is higher. Thus, the smoothing in the MUSCAT algorithm (resulting from the interpolation of data onto a regular grid) results in similar $\sigma(D)$ for the horizontal wind and higher values of $\sigma(D)$ for the vertical wind.

Three additional scan strategies were introduced, each of which are divided into subtypes. First, a volume scan strategy is applied during the T-REX campaign (TX); the second strategy ensures volume coverage based on interpolation radii of the retrieval algorithm (VC); and the third is a strategy where the volume is scanned in a sinusoidal wave pattern (SW). The strategies are analyzed with respect to three criteria: deviations of retrieved winds from original fields, scan duration, and size of the retrieved fields. Considering these criteria, VC scans are found to compromise best between minimal differences and the minimal scan duration, and the maximum size of the retrieved field. Reducing the calculated angles between successive PPIs of the VC scans shrinks differences and increases field size at the expense of scan duration. If only total VC scans (i.e., without interlacing) are used, an overlap of the interpolation ellipsoids by reducing the calculated elevation angles up to 20%–40% is most meaningful. Beyond that increase in overlap, the improvements do not compensate for the lengthening of the scan duration anymore. In the case of using an interlaced scanning strategy in order to profit from each of the quickly scanned two halves, the angles between successive PPIs should be reduced by 40%–50% at least, depending on the actual measurement range. Please note that the TX-m scan pattern, applied during the field campaign, ranks among the best regarding the accuracy of the retrieved wind and the field size, making it an appropriate strategy for *slowly* changing flow situations. Indeed, its scan duration is among the longest of the studied strategies.

TABLE 2. Recommended scanning strategies, depending on the expected temporal variability τ (min) of the wind situation and actual measurement range R [km; horizontally (h) and vertically (v)]; N is the size of the retrieved field (%) relative to the reference scan over flat terrain, and T is the scan duration (min).

Maximum range	Scan ($\tau < 10$)	N	T	Scan ($\tau \gtrsim 10$)	N	T
	VC-h1–50 with	57	4.2	VC-c-30	77	6.2
$R \approx h4v4$	VC-h2–50	67	4.2	VC-c-40	78	7.3
	→VC-c-50	80	8.4			
				TX-m6	89	10.5
	VC-h1–40 with	82	7.3	VC-c-20	87	10.5
$R \approx h8v4$	VC-h2–40	78	6.2	VC-c-30	92	11.5
	→VC-c-40	93	13.6	VC-c-40	93	13.6
	VC-h1–40 with	84	8.4	VC-c-0	89	9.4
$R \approx h8v6$	VC-h2–40	90	7.3	VC-c-10	90	10.5
	→VC-c-40	95	15.7	VC-c-20	89	11.5

In future field campaigns that are designed to derive 3D wind fields from dual-Doppler lidar measurements, the scanning strategies should be chosen depending on actual maximum ranges and the temporal variability of the phenomenon to be observed, in order to maximize spatial coverage and minimize spatial and temporal smoothing of the retrieved fields. Recommendations for the scan pattern trying to compromise best between the environmental situation and the requirements of the operator are summarized in Table 2. In general, interlaced VC-h scans are best because they still have an acceptable accuracy and size of covered volume for quickly changing situations and the best accuracy and coverage when combined for more stationary situations. Note that wind fields retrieved from dual-Doppler lidar volume scans will always experience both spatial and temporal smoothing, especially in wind situations changing faster than 5–10 min. In the case of low horizontal and vertical maximum ranges of about 4 km and wind situations changing within 5 min, the scan pattern according to Eq. (1), with

calculated angles reduced by (at least) 50% and applied in an interlaced mode (i.e., VC-h1–50, together with VC-h2–50), clearly optimizes the spatial coverage, scan duration, and quality of the derived wind data. Each half takes less than 5 min, and the composite scan VC-c-50 (10 min) reveals almost the same results as those of the high-resolution benchmark scan (which takes more than 500 min). For less variable wind situations, the scan durations of the noninterlaced strategies VC-c-30 and VC-c-40 have to be traded off against their spatial coverage and smoothing. For larger horizontal but low vertical maximum ranges, the VC-c-40 scan pattern in the interlaced mode is most appropriate in variable wind situations. For more stationary conditions, the TX-m6, VC-c-20, VC-c-30, or VC-c-40 (in the noninterlaced mode) can provide satisfying data for wind retrieval. In cases of large horizontal and vertical maximum ranges and wind situations changing faster than 10 min, the VC-c-40 applied in interlaced mode should be chosen. For less variable wind situations, the noninterlaced VC-c-0, VC-c-10, or VC-c-20 should be used, depending on weighting of the scan speed versus the smoothing and spatial coverage.

Acknowledgments. This study was supported by the Austrian Science Fund FWF under Grant P18940. Thanks to Oliver Reitebuch and Martin Weissman of DLR for answering all our questions about the DLR Doppler lidar. Author FKC received support from National Science Foundation Grant ATM-0645784.

REFERENCES

Banta, R. M., L. D. Olivier, E. T. Holloway, R. A. Kropfli, B. W. Bartram, R. E. Cupp, and M. J. Post, 1992: Smoke-column observations from two forest fires using Doppler lidar and Doppler radar. *J. Appl. Meteor.,* **31,** 1328–1349.

Bousquet, O., and M. Chong, 1998: A Multiple-Doppler Synthesis and Continuity Adjustment Technique (MUSCAT) to recover wind components from Doppler radar measurements. *J. Atmos. Oceanic Technol.,* **15,** 343–359.

Browning, K. A., and R. Wexler, 1968: The determination of kinematic properties of a wind field using Doppler radar. *J. Appl. Meteor.,* **7,** 105–113.

Caillault, K., and Y. Lemaitre, 1999: Retrieval of three-dimensional wind fields corrected for the time-induced advection problem. *J. Atmos. Oceanic Technol.,* **16,** 708–722.

Calhoun, R., R. Heap, M. Princevac, R. Newsom, H. Fernando, and D. Ligon, 2006: Virtual towers using coherent Doppler lidar during the Joint Urban 2003 dispersion experiment. *J. Appl. Meteor. Climatol.,* **45,** 1116–1126.

Chai, T., C.-L. Lin, and R. Newsom, 2004: Retrieval of microscale flow structures from high-resolution Doppler lidar data using an adjoint model. *J. Atmos. Sci.,* **61,** 1500–1520.

Chong, M., and J. Testud, 1996: Three-dimensional air circulation in a squall line from airborne dual-beam Doppler radar data: A test of coplane methodology software. *J. Atmos. Oceanic Technol.,* **13,** 36–53.

——, and S. Cosma, 2000: A formulation of the continuity equation of MUSCAT for either flat or complex terrain. *J. Atmos. Oceanic Technol.,* **17,** 1556–1565.

——, and O. Bousquet, 2001: On the application of MUSCAT to a ground-based dual-Doppler radar system. *Meteor. Atmos. Phys.,* **78,** 133–139.

Drechsel, S., M. Chong, G. J. Mayr, M. Weissmann, R. Calhoun, and A. Dörnbrack, 2009: Three-dimensional wind retrieval: Application of MUSCAT to dual-Doppler lidar. *J. Atmos. Oceanic Technol.,* **26,** 635–646.

Grubišić, V., and Coauthors, 2008: The Terrain-Induced Rotor Experiment: A field campaign overview including observational highlights. *Bull. Amer. Meteor. Soc.,* **89,** 1513–1533.

Hill, M., R. Calhoun, H. Fernando, A. Wieser, A. Dörnbrack, M. Weissmann, G. Mayr, and R. Newsom, 2010: Coplanar Doppler lidar retrieval of rotors from T-REX. *J. Atmos. Sci.,* **67,** 713–729.

Intrieri, J. M., A. J. Bedard Jr., and R. M. Hardesty, 1990: Details of colliding thunderstorm outflows as observed by Doppler lidar. *J. Atmos. Sci.,* **47,** 1081–1099.

Meischner, P., Ed., 2004: *Weather Radar: Principles and Advanced Applications*. Springer, 337 pp.

Newsom, R., R. Calhoun, D. Ligon, and J. Allwine, 2008: Linearly organized turbulence structures observed over a suburban area by dual-Doppler lidar. *Bound.-Layer Meteor.,* **127,** 111–130.

Shapiro, A., P. Robinson, J. Wurman, and J. Gao, 2003: Single-Doppler velocity retrieval with rapid-scan radar data. *J. Atmos. Oceanic Technol.,* **20,** 1758–1775.

Shun, C. M., and P. W. Chan, 2008: Applications of an infrared Doppler lidar in detection of wind shear. *J. Atmos. Oceanic Technol.,* **25,** 637–655.

Vasiloff, S. V., R. J. Doviak, and M. T. Istok, 1987: Weather radar interlaced scanning strategy. *J. Atmos. Oceanic Technol.,* **4,** 245–249.

Weitkamp, C., Ed., 2005: *Lidar: Range-Resolved Optical Remote Sensing of the Atmosphere*. Springer Series in Optical Sciences, Vol. 102, Springer, 460 pp.

Yu, T., M. B. Orescanin, C. D. Curtis, D. S. Zrnić, and D. E. Gorsyth, 2007: Beam multiplexing using the phased-array weather radar. *J. Atmos. Oceanic Technol.,* **24,** 616–626.